Impact of Arctic Sea Ice Interannual Variation on Nonmonsoonal Winter Precipitation over the Eurasian Continent

QIFENG QIAN,[a] XIAOJING JIA,[b] RENGUANG WU,[b] AND MIN WANG[a]

[a] *Zhejiang Institute of Meteorological Sciences, Hangzhou, China*
[b] *Key Laboratory of Geoscience Big Data and Deep Resource of Zhejiang Province, School of Earth Sciences, Zhejiang University, Hangzhou, China*

(Manuscript received 17 August 2022, in final form 8 February 2023, accepted 21 February 2023)

ABSTRACT: The present study analyzes the impact of interannual variation in autumn (September–November) Arctic sea ice concentration (SIC) on early winter (November–January) precipitation over nonmonsoonal Eurasian (NME) regions based on both observations and numerical model experiments. An energy budget analysis shows that negative autumn SIC anomalies in the Beaufort–Chukchi–East Siberian Seas (BCES) induce heating in the overlying atmospheric column, which excites a Rossby wave that propagates from the BCES through the Atlantic Ocean to the mid- and high-latitude Eurasian continent. This Rossby wave obtains energy from the mean flow by both baroclinic and barotropic energy conversions. In comparison, the baroclinic energy conversion is more important than the barotropic energy conversion. The low-level anomalous cyclone and anticyclone of the Rossby wave dominate the eastern North Atlantic Ocean–southern Europe and western Russia, respectively. Anomalous westerly wind along the south flank of the anomalous cyclone transports moisture from the North Atlantic Ocean to the continent, resulting in a water vapor flux convergence and positive precipitation anomaly over southern Europe in early winter. Pronounced anomalous northerly winds in the eastern part of the western Russian anticyclone cause negative precipitation anomalies over vast regions of central Asia and the west Siberian plain in early winter. The Rossby wave ray tracing experiment and numerical sensitivity experiments support the above BCES SIC–NME precipitation connection.

KEYWORDS: Arctic; Sea ice; Climate variability; Interannual variability

1. Introduction

Different from the climate over monsoonal areas, which is impacted by seasonal reversals of prevailing wind directions between summer and winter, the climate over the mid- and high-latitude central–western Eurasian continent is mainly dominated by nonmonsoonal airflow (e.g., Li and Zeng 2005, their Fig. 2; An et al. 2015, their Fig. 2). In both summer and winter, westerly winds blow from the mid- and high-latitude North Atlantic Ocean to the downstream Eurasian continent and control the climate over vast regions from the northern Mediterranean Sea to northern China. Far from the ocean, most of these nonmonsoonal Eurasian (NME) regions (30°–60°N, 30°–105°E; Qian et al. 2021) are characterized by arid or semiarid climates (e.g., Li et al. 2015).

Due to the infertile land and sparse vegetation cover, the water resources in the NME region are important for ecosystems, agriculture, irrigation, economic activity, social stability, and people's lives. Previous studies have noted that central Eurasia has warmed by twofold compared with the global average in the past century (e.g., Giorgi 2006; Chen et al. 2009; Huang et al. 2016; Hu et al. 2016), and the temperature over these regions might continue increasing at a relatively high rate in the future (e.g., Christensen et al. 2013; Peng et al. 2020). The increase in temperature will lead to the melting of snow cover and the shrinkage of glaciers over central Asia (e.g., Sorg et al. 2012). Some studies have revealed that the annual precipitation over the central Eurasian continent has increased in the past several decades and might continue to increase in the future (e.g., Huang et al. 2012, 2014; Jiang et al. 2020). However, such enhanced annual rainfall is reported without distinguishing plausible differences among the seasons (e.g., Huang et al. 2012, 2014; Jiang et al. 2020).

Previous studies have noted that the variation in precipitation over the central Eurasian continent can be affected by the variation of the subtropical westerly jet (e.g., Zhang et al. 2006; Zhao et al. 2014; Fallah et al. 2016), the variation in Tibetan Plateau thermal conditions (Yao and Chen 2015), Asian polar vortices (Yao and Chen 2015), and continental wave train patterns related to the North Atlantic Ocean sea surface temperature (SST) (e.g., Wu et al. 2016; Jia et al. 2018). In addition, snow cover and sea ice can also affect the Eurasian continental climate variations by modulating atmospheric circulations (e.g., Li and Wang 2012; Chen et al. 2016; Wang et al. 2019; Ding et al. 2021). For example, the Arctic sea ice, which is an important component of the global climate system, can affect the local energy balance through the ice albedo effect (Curry et al. 1995). The Arctic sea ice can modulate the exchange of energy between the overlying atmosphere and the ice-covered ocean (e.g., Serreze et al. 2007; Budikova 2009; Vihma et al. 2020; Gao et al. 2015) and impose climate impacts on the mid- and low latitudes by regulating atmospheric general circulation (e.g., Deser et al. 2000; Alexander et al. 2004; Dethloff et al. 2006; Jaiser et al. 2012; Chen and Wu 2018).

Supplemental information related to this paper is available at the Journals Online website: https://doi.org/10.1175/JCLI-D-22-0634.s1.

Corresponding author: Xiaojing Jia, jiaxiaojing@zju.edu.cn

DOI: 10.1175/JCLI-D-22-0634.1

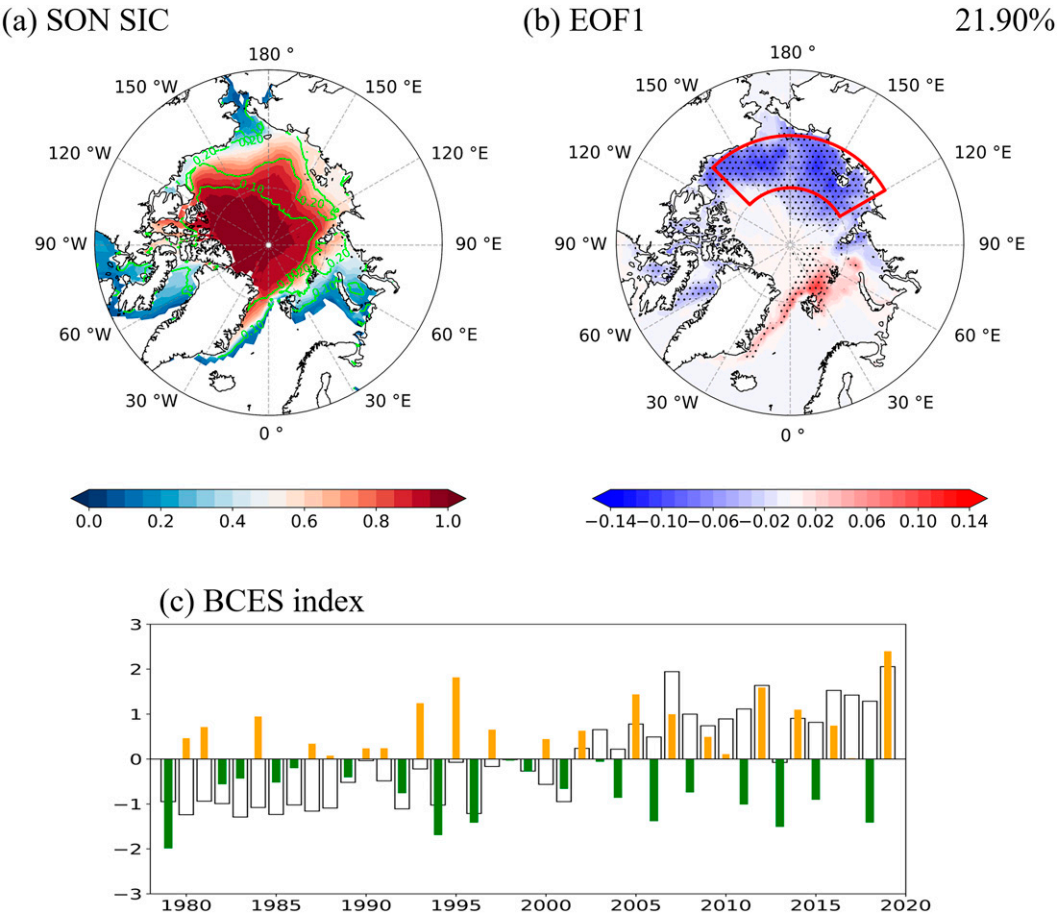

FIG. 1. (a) Spatial distribution of the SON Arctic SIC (shading; unit: 1) and corresponding interannual standard deviation (contours) for the 1979–2019 period. (b) Distribution of the EOF1 of the filtered SON SIC for the 1979–2019 period. The percentage on the top right is the percent variance explained by the EOF1 mode. Stippled regions denote the 90% confidence level. The red box represents the key region (70°–80°N, 135°W–120°E). (c) The transparent bars represent the normalized BCES index obtained by the area-weighted mean of the SON SIC over the key region in (b), and the solid bars denote the filtered BCES index with periods longer than 10 years removed.

In recent decades, a fast decrease in the Arctic sea ice accompanied by the Arctic warming has received increasing attention (e.g., Stroeve and Notz 2018). In particular, autumn Arctic sea ice shows the largest decreasing rate, reaching a record low (−40%) in 2012 (IPCC 2019). Many studies have investigated the climate impacts of autumn Arctic sea ice anomalies on the climate over the Eurasian continent in the following seasons (Francis et al. 2009; Wu et al. 2011; Hopsch et al. 2012; Jaiser et al. 2012; Chen et al. 2014; Nakamura et al. 2015; Chen and Wu 2018), with a focus on the subsequent winter temperature, extreme cold events, and snowstorms (e.g., Francis and Vavrus 2012; Liu et al. 2012; Tang et al. 2013; Wu et al. 2013; Francis and Vavrus 2015; Wu et al. 2017; Ding et al. 2021). These studies examined how the loss of autumn and early winter sea ice over the Arctic, especially over the Barents–Kara Seas, affects the Eurasian temperature variability via stratospheric processes (e.g., Peings and Magnusdottir 2014; Sun et al. 2015; Chen and Wu 2018; Zhang and Screen 2021). Blackport and Screen (2019) further pointed out that winter atmospheric circulation anomalies mainly respond to concurrent winter sea ice loss rather than autumn sea ice loss. However, most of the above studies investigated the climate impacts of autumn Arctic sea ice anomalies on the subsequent seasonal temperature, while fewer studies have investigated the climate impacts on the subsequent seasonal precipitation. Li and Wang (2012) revealed that autumn Arctic sea ice anomalies in the Kara–Laptev Seas can modulate the winter Northern Hemisphere Annular Mode and further affect winter precipitation over the Eurasian continent. He et al. (2022) revealed that autumn sea ice variation on an interdecadal time scale affects the subsequent winter temperature and precipitation over the Eurasian continent by weakening the stratospheric polar vortex. In our recent work (Qian et al. 2021), four machine learning models were constructed to perform seasonal forecast experiments for winter precipitation over the NME, and we noticed that the Arctic sea ice over the Beaufort–Chukchi Seas in the previous autumn plays the most essential role in seasonal forecasts. However, the reason behind the contribution of the Arctic sea ice to the improved seasonal forecast skill remains

unknown. In the current study, we revealed that the interannual variation in autumn sea ice over the Beaufort–Chukchi–East Siberian Seas (BCES) can affect the subsequent winter precipitation variation over the NME. The possible physical mechanisms are investigated through observational analysis and numerical model experiments.

The rest of the paper is organized as follows. Section 2 describes the data, methods, and numerical model used in this study. Section 3 documents the climatological characteristics of autumn Arctic sea ice. Section 4 presents the climate impacts of autumn Arctic sea ice anomalies on the NME precipitation and the possible mechanisms. Section 5 summarizes the main results of this study.

2. Data, methods, and numerical model

a. Data

The datasets used in the present work are described as follows:

1) The monthly land rainfall data with a horizontal resolution of 0.5° × 0.5° (version TS4.05) from 1901 to 2020 are accessed from the Climate Research Unit (CRU) of the University of East Anglia (Harris et al. 2014).
2) The monthly SST and sea ice concentration (SIC) data gridded at 1° × 1° resolution with a time span from 1870 to 2020 are obtained from the Met Office Hadley Centre (Rayner et al. 2003).
3) The National Centers for Environmental Prediction (NCEP)–U.S. Department of Energy (DOE) AMIP-II reanalysis (Kanamitsu et al. 2002), available from January 1979 to the present with a 2.5° × 2.5° horizontal resolution, provides monthly climatological fields at various pressure levels, including air temperature, geopotential height, horizontal wind velocities, and relative humidity. Surface monthly mean climate variables, including 2-m air temperature, surface latent heat flux, surface sensible heat flux, downward and upward solar radiation fluxes, downward and upward longwave radiation fluxes, and precipitation rate, are also obtained from the NCEP–DOE AMIP-II reanalysis. These surface variables are on T62 Gaussian grids. The daily geopotential height data of the NCEP–DOE AMIP-II reanalysis with a 2.5° × 2.5° horizontal resolution are also used to investigate the stratospheric coupling process.

In this study, we focus on the time period from 1979 to 2020 and the seasons of autumn [September–November (SON)], late autumn [October–December (OND)], and early winter [November–January (NDJ)]. Here, we define the early winter of 1979 as the 3 months from November 1979 to January 1980 following Wang et al. (2017). Monthly data are converted to seasonal data accordingly and used to perform the analysis in the following text.

b. Methods

In this study, the interannual variation in the dataset is obtained by applying a 10-yr high-pass Fourier filter. A brief discussion of the application of the high-pass filter and time scale can be found in section 5 of the online supplemental material. Other statistical methods, including linear regression, the Student's t test, and empirical orthogonal function (EOF) analysis, are also used in this study. The degree of freedom is calculated following Bretherton et al. (1999) when filtered time series are used in the statistical analysis. The criteria proposed by North et al. (1982) are used to determine whether one EOF mode is well separated from the others. In the following text, the anomaly of a variable is defined as the deviation from its climatological basic states from 1979 to 2020.

The wave activity flux (WAF) proposed by Takaya and Nakamura (2001) is used in this study to investigate Rossby wave propagation. This WAF can capture instantaneous wave propagation, which makes it suitable for both migratory and stationary quasigeostrophic waves on a zonally asymmetric

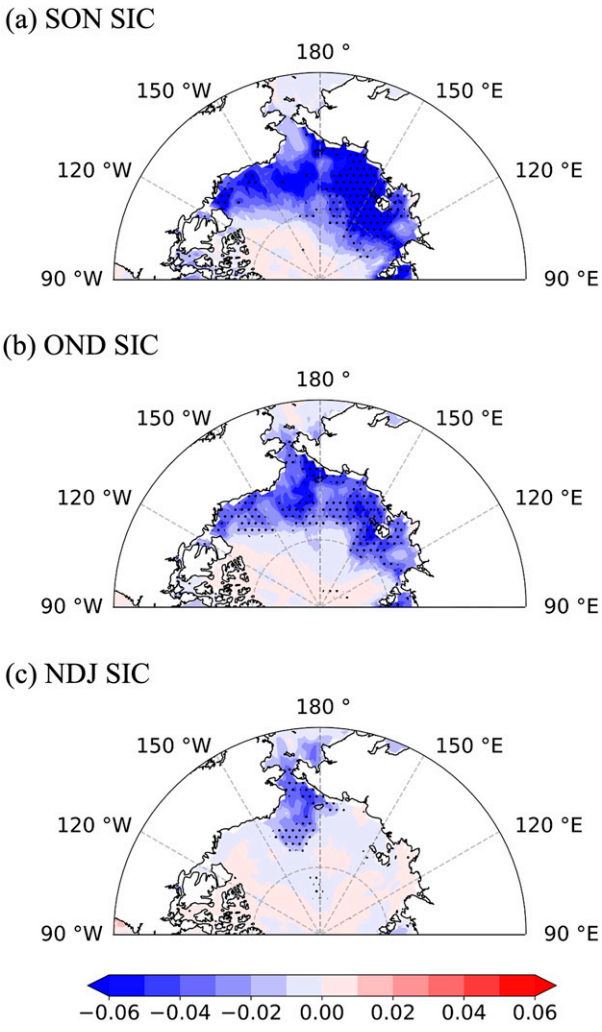

FIG. 2. Anomalies of (a) SON, (b) OND, and (c) NDJ SIC (unit: 1) obtained by linear regression onto the IBCES index. Stippled regions denote anomalies significant at the 90% confidence level.

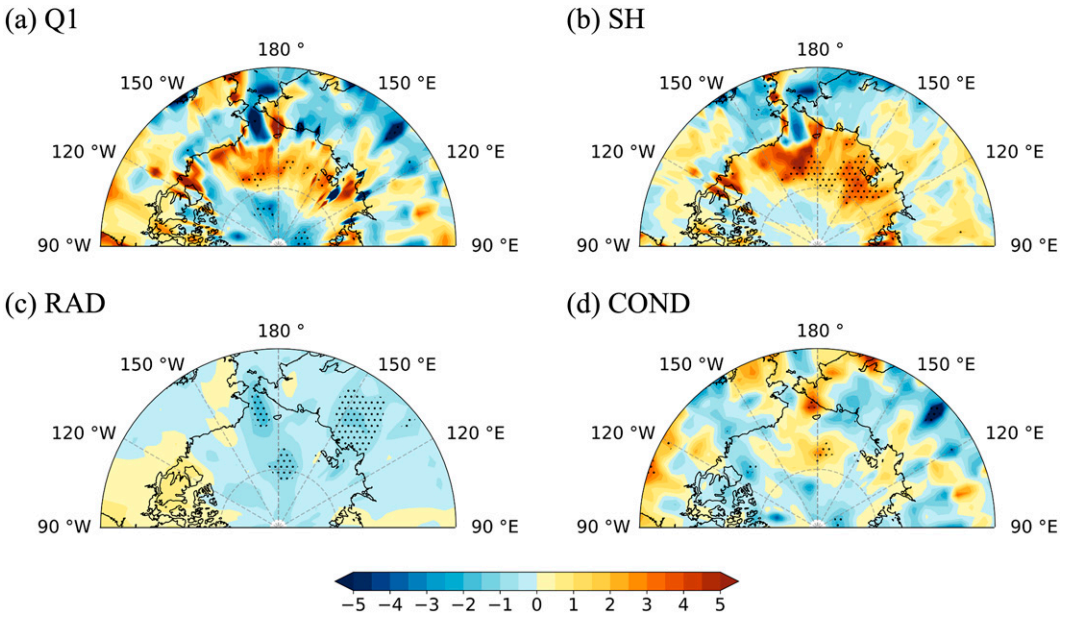

FIG. 3. Anomalies of SON (a) Q1 (unit: W m^{-2}), (b) SH (unit: W m^{-2}), (c) RAD (unit: W m^{-2}) and (d) COND (unit: W m^{-2}) obtained by linear regression onto the IBCES index. Stippled regions denote anomalies significant at the 90% confidence level.

basic flow. Only the horizontal components of this WAF are used in this study. The formation of the horizontal component of the WAF $\mathbf{W}$ can be expressed as follows:

$$\mathbf{W} = \frac{1}{2|\mathbf{U}|}\begin{bmatrix} U(\psi_x'^2 - \psi'\psi_{xx}') + V(\psi_x'\psi_y' - \psi'\psi_{xy}') \\ U(\psi_x'\psi_y' - \psi'\psi_{xy}') + V(\psi_y'^2 - \psi'\psi_{yy}') \end{bmatrix}, \tag{1}$$

where ψ represents the streamfunction and U and V represent the horizontal components of the basic flow wind vector $\mathbf{U}(U, V)$, respectively. The primes denote perturbations on the basic flow, and the subscripts denote partial derivatives.

The total column atmospheric heat source/sink (Q1) proposed by Zhao and Chen (2001) is applied to investigate the effect of sea ice anomalies on the overlying atmosphere. Q1 can be calculated as follows:

$$\mathrm{Q1} = \mathrm{SH} + \mathrm{RAD} + \mathrm{COND}, \tag{2}$$

where SH is the sensible heat flux at the surface, RAD represents the net radiation in an atmospheric column, and COND denotes the latent heat induced by condensation. When Q1 is positive (negative), the atmospheric column is a heat source (sink).

To investigate the source of Rossby waves, we adopt the vorticity forcing formulated by Sardeshmukh and Hoskins (1988) in this study. The Rossby wave sources (RWSs) are related to the variation in vorticity in classic Rossby wave theory, which can be described by a forced barotropic vorticity equation (Sardeshmukh and Hoskins 1988):

$$\left(\frac{\partial}{\partial t} + \mathbf{V}_\psi \cdot \boldsymbol{\nabla}\right)\xi_a = S, \tag{3}$$

$$S = -\xi_a D - \mathbf{V}_\chi \cdot \boldsymbol{\nabla}\xi_a = -\boldsymbol{\nabla} \cdot (\mathbf{V}_\chi \xi_a), \tag{4}$$

where S is the source/sink of the Rossby waves, which also represents the vorticity forcing; ξ_a is the absolute vorticity; D denotes the divergence; $\mathbf{V}_\psi = \mathbf{k} \times \boldsymbol{\nabla}\psi$ represents the rotational wind; and $\mathbf{V}\chi = \boldsymbol{\nabla}\chi$ denotes the divergent wind.

To further investigate Rossby waves, the barotropic energy conversion (CK) and baroclinic energy conversion (CP) formulated by Kosaka and Nakamura (2006) are calculated as follows:

$$\mathrm{CK} = \left[\frac{v'^2 - u'^2}{2}\left(\frac{\partial \overline{u}}{\partial x} - \frac{\partial \overline{v}}{\partial y}\right) - u'v'\left(\frac{\partial \overline{u}}{\partial y} + \frac{\partial \overline{v}}{\partial x}\right)\right], \tag{5}$$

$$\mathrm{CP} = -\left[\frac{f}{\sigma}v'T'\frac{\partial \overline{u}}{\partial p} + \frac{f}{\sigma}u'T'\frac{\partial \overline{v}}{\partial p}\right], \tag{6}$$

$$\sigma = \frac{R\overline{T}}{c_p p} - \frac{d\overline{T}}{dp}, \tag{7}$$

where u', v', and T' denote the perturbed zonal and meridional wind and temperature, respectively; $\overline{u}$, $\overline{v}$, and $\overline{T}$ represent the basic states of the zonal and meridional wind and temperature, respectively; f represents the Coriolis parameter; c_p is the specific heat at a constant pressure; and the square brackets represent a vertical integration taken from the surface to the top of the atmosphere.

To track the path of Rossby waves, the Rossby wave ray tracing algorithm proposed by Karoly (1983) is used in this study. The path of a wave ray can be obtained by integrating

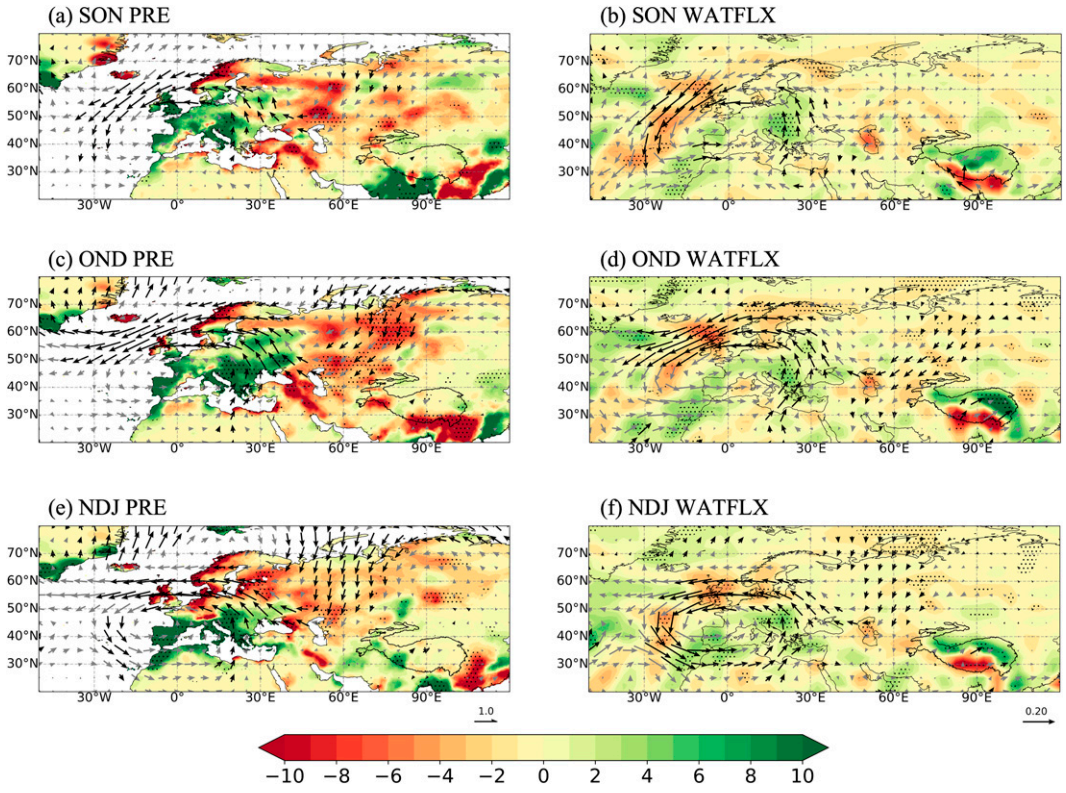

FIG. 4. (a),(b) SON, (c),(d) OND, and (e),(f) NDJ (a),(c),(e) precipitation anomalies (shading; unit: mm) and 850-hPa wind (black vectors; unit: m s^{-1}) and (b),(d),(f) column water vapor flux from 1000 to 10 hPa (vectors; unit: 10^2 kg·m^{-1}·s^{-1}) and corresponding divergence (shading; unit: 10^2 kg·m^{-1}·s^{-1}) obtained by linear regression onto the IBCES index. Stippled regions represent anomalies significant at the 90% confidence level. Black vectors represent vector anomalies significant at the 90% confidence level. The red rectangle box denotes the NME region (30°–60°N, 30°–105°E).

the following equations for the ray path (x, y) and wavenumber (k, l) under the Mercator projection:

$$\frac{dx}{dt} = u_g = \overline{u}_M + \frac{[(k^2 - l^2)\overline{q}_y - 2kl\overline{q}_x]}{\mathbf{K}^4}, \tag{8}$$

$$\frac{dy}{dt} = v_g = \overline{v}_M + \frac{[2kl\overline{q}_y + (k^2 - l^2)\overline{q}_x]}{\mathbf{K}^4}, \tag{9}$$

$$\frac{d_g k}{dt} = -\frac{\partial \omega}{\partial x} = -k\overline{u}_x - l\overline{v}_x + \frac{\overline{q}_{xy}k - \overline{q}_{xx}l}{\mathbf{K}^4}, \tag{10}$$

$$\frac{d_g l}{dt} = -\frac{\partial \omega}{\partial y} = -k\overline{u}_y - l\overline{v}_y + \frac{\overline{q}_{yy}k - \overline{q}_{xy}l}{\mathbf{K}^4}, \tag{11}$$

$$\omega = \overline{u}_M k + \overline{v}_M l + \frac{(\overline{q}_x l - \overline{q}_y k)}{\mathbf{K}^4}, \tag{12}$$

where $\overline{u}_M$ and $\overline{v}_M$ denote the basic states of the zonal and meridional winds in the Mercator projection, respectively; $\mathbf{K} = (k, l)$ denotes the wavenumber; $\overline{q}$ is the absolute vorticity of the basic states; ω is the dispersion relationship; and the subscripts x and y represent partial derivatives in the zonal and meridional directions, respectively. The details of the ray tracing experiment are described as follows:

1) The climatological means of autumn 200-hPa horizontal velocities obtained from the NCEP–DOE AMIP-II reanalysis are employed as the basic states.
2) The ray tracings are initialized with zonal wavenumbers 1–7 following Shaman and Tziperman (2005) at forcing sites near the Bering Strait.
3) To make the result more robust, grid points that fall within 65.0°–72.5°N, 132.5°W–180.0° (red box in Fig. 7) are assigned a perturbation according to the distribution of RWS anomalies (Fig. 7; Li et al. 2015; Yiu and Maycock 2019, 2020), and each perturbation is tracked independently.
4) The integration time for the ray path is 20 days.

c. Numerical model

The sensitivity experiments performed in this study are conducted using the National Center for Atmospheric Research (NCAR) Community Atmosphere Model, version 5.2 (CAM5.2),

which is the atmospheric component of the Community Earth System Model (CESM). The finite-volume dynamic core with a horizontal resolution of 1.9° × 2.5° and 30 vertical levels in hybrid pressure–sigma coordinates with a top at 2.255 hPa is used in this study (Neale et al. 2010). The physical parameterization schemes of CAM include a double-moment microphysics scheme (Morrison and Gettelman 2008), a cloud macrophysics scheme (Park et al. 2014), a deep convection scheme (Zhang and McFarlane 1995), a shallow convection scheme (Park and Bretherton 2009), a moist turbulent scheme (Bretherton and Park 2009), and the Rapid Radiative Transfer Model for longwave and shortwave radiative transfer (Iacono et al. 2008). As a complex numerical model, CAM5 is widely used in climate research and can help to understand and verify atmospheric responses to variations in sea ice (e.g., Ding et al. 2021; Peings and Magnusdottir 2014). In this study, we perform two numerical experiments using CAM to examine the role of the BCES SIC forcing on the atmosphere. In the first experiment, climatological monthly SIC and SST for the analysis period are specified in the model, and the results of this experiment serve as a reference (control experiment). In the sensitivity experiment, the SIC forcing (see supplemental material section 4) is composed of climatological monthly SIC and the SIC anomalies in September, October, and November over BCES (red box in Fig. 1b), which are determined according to the distribution of SIC anomalies obtained by linear regression against the interannual component of the BCES index (IBCES; Ding et al. 2021). The SST in the sensitivity experiment is the same as that in the control experiment. The difference between the sensitivity experiment and the control experiment represents the atmospheric response to the SIC anomalies in BCES. In each experiment, CAM is integrated for 220 years following the suggestion of the Polar Amplification Model Intercomparison Project (PAMIP; Ogawa et al. 2018; Smith et al. 2019; Siew et al. 2020; Peings et al. 2021). The first 20 years of integration are treated as the spinup period, and the last 200 years are used for analysis.

3. Climatological characteristics of autumn Arctic SIC

In this section, the characteristics of the climatological mean and interannual variation in the autumn SIC in the Arctic region are first examined. The climatological mean SIC (Fig. 1a, color shading) shows that in autumn, vast regions of the Arctic are covered by sea ice, with the center close to the North Pole. The standard deviation of the SIC (Fig. 1a, contours) shows large values in the BCES, which is the marginal Arctic Ocean. The regions near the North Pole with large values of climatological mean SIC have small values of standard deviation as the SIC is perennial there, consistent with previous studies (Wu et al. 2011; Ding et al. 2021).

EOF analysis is then conducted on the Arctic SIC to obtain the dominant mode of the autumn SIC variations. The spatial distribution of the leading EOF mode (EOF1) of the SIC is presented in Fig. 1b, obtained by regressing the autumn SIC onto the corresponding principal component (PC1; not shown) of EOF1. EOF1 accounts for 21.90% of the autumn SIC variance during the analysis period and is well separated from the other EOF modes according to the criteria of North

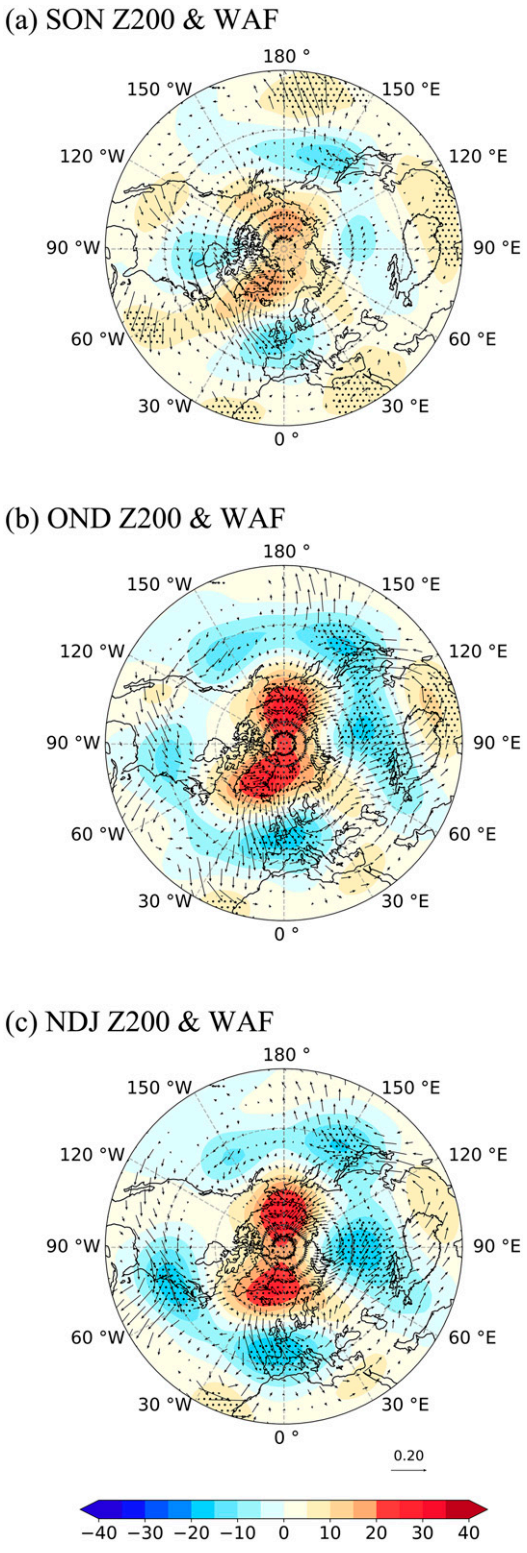

FIG. 5. Anomalies of (a) SON, (b) OND, and (c) NDJ 200-hPa geopotential height (shading; unit: gpm) and the corresponding wave activity flux (vectors; unit: $m^2\ s^{-2}$) obtained by linear regression onto the IBCES index. Stippled regions denote the 90% confidence level.

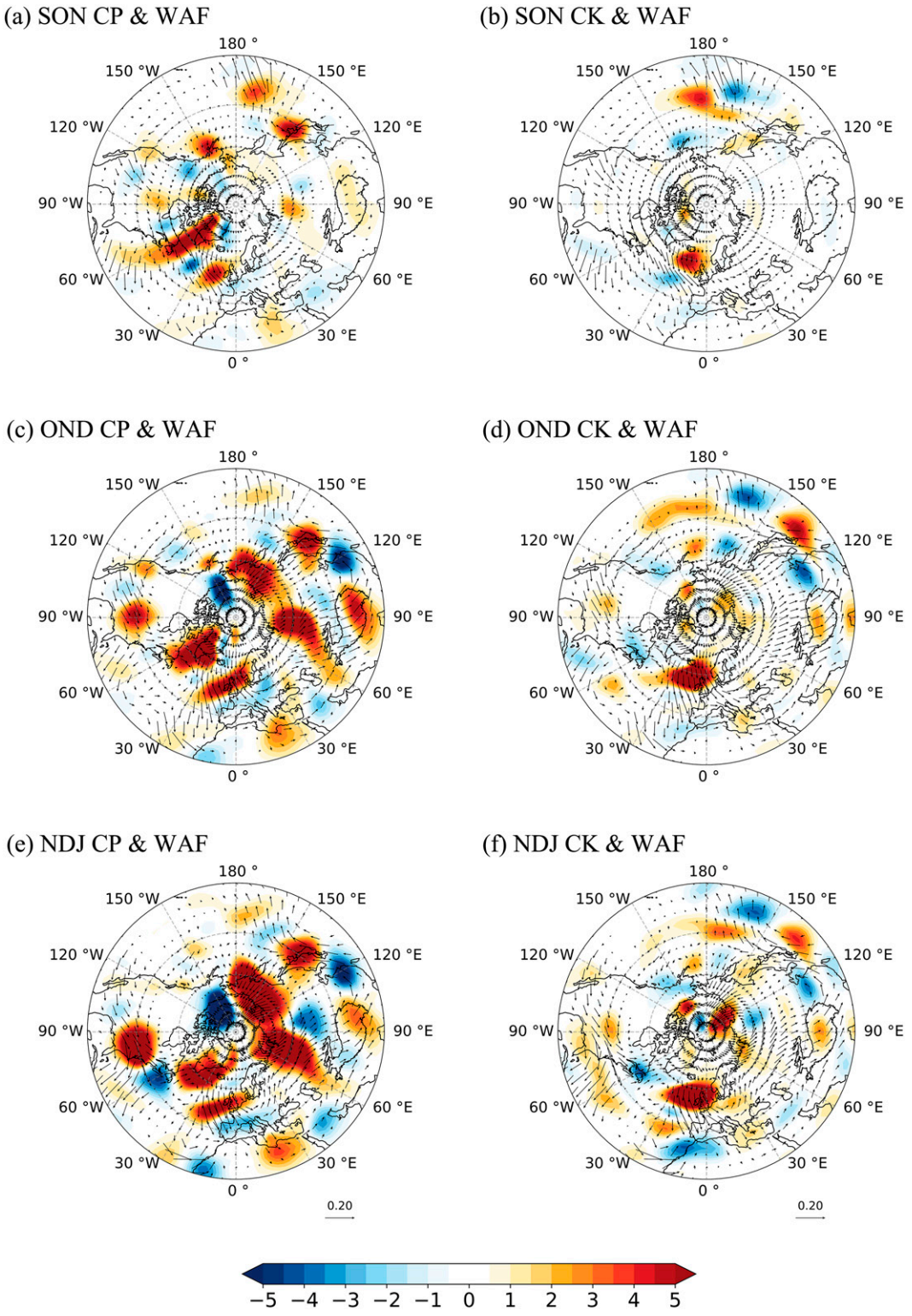

FIG. 6. Anomalies of (a),(b) SON, (c),(d) OND, and (e),(f) NDJ vertically integrated (a),(c),(e) baroclinic energy conversion (shading; unit: 10^{-1} W m^{-2}) and (b),(d),(f) barotropic energy conversion (shading; unit: 10^{-3} W m^{-2}) obtained by linear regression onto the IBCES index. Overlaid black vectors represent wave activity flux (unit: m^2 s^{-2}) at 200 hPa.

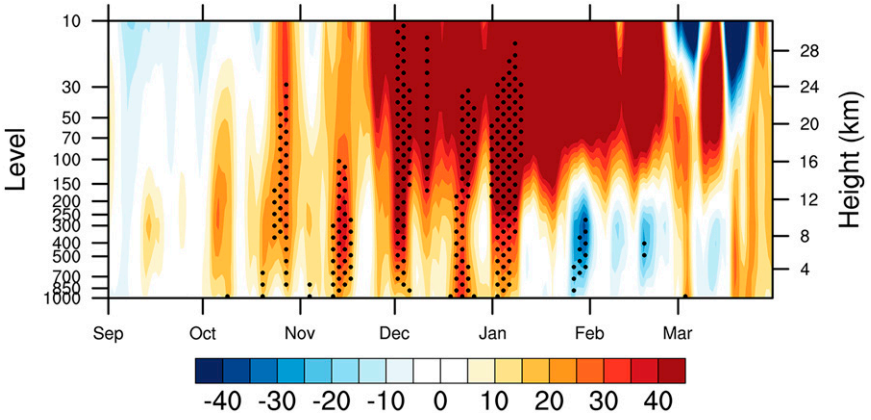

FIG. 7. Time–height cross sections of area–mean geopotential height anomalies (shading; unit: gpm) over the Arctic region (70°–90°N, 180°W–180°E) regressed upon IBCES.

et al. (1982). As shown in Fig. 1b, EOF1 is characterized by large loadings in the BCES. Significant SIC loadings with opposite signs are observed in the Barents–Kara Seas. The magnitudes of the interannual variation in SIC in BCES are much larger than those in the Barents–Kara Seas. Therefore, an SIC index is constructed by averaging the SIC anomalies over the BCES region (denoted by the red box in Fig. 1b) to represent the interannual variation in the SIC in the BCES. For convenience, this SIC index is normalized and multiplied by −1 and is defined as the BCES index. Here, a positive (negative) index represents decreased (increased) autumn SIC in these regions. The BCES index (Fig. 1c, transparent bars) and its interannual component (Fig. 1c, solid bars) are shown in Fig. 1c. The BCES index is dominated by negative values before 2001 and positive values after 2002, suggesting that the autumn SIC in BCES has a pronounced decreasing trend, which is consistent with previous studies (e.g., Ding et al. 2021). The current work focuses on the interannual variation, and therefore, a 10-yr high-pass Fourier filter is applied to the BCES index, and the interannual component of the BCES index is used in the following analysis to represent the interannual variation in autumn SIC in the BCES region.

The SIC anomalies associated with the interannual variation in BCES SIC from autumn to early winter are obtained by linear regression onto the IBCES index (Fig. 2). Significant negative SIC anomalies are observed in BCES in autumn (Fig. 2a), suggesting that the IBCES index can well represent the autumn SIC variation in the key region (red box in Fig. 1b). The significant negative SIC anomalies in the BCES persist in OND (Fig. 2b). The anomalous SIC decays quickly in the following early winter but can still be observed with significance in the Chukchi Sea (Fig. 2c). Figure 2 reveals that the autumn BCES SIC anomalies can persist until early winter. This indicates a possible persistent forcing of the SIC on the overlying atmosphere and perhaps a persistent impact on the climate in the following early winter.

To understand how the autumn BCES SIC impacts the climate, the SIC-related changes in the local energy budget are investigated by examining the anomalies of autumn SAT, SST, and surface heat fluxes associated with SIC variation in BCES obtained by regressing these variables onto IBCES (section 1 in supplemental material). Overall, we found that negative SIC anomalies in BCES lead to pronounced anomalous warming in the near-surface air (supplemental Fig. 1f).

The warming effect of the negative autumn BCES SIC anomalies on the local atmosphere is further examined using the total heat source anomalies (Q1), which are obtained by linear regression (Fig. 3a). Significant positive Q1 anomalies are observed to be associated with the IBCES, indicating that the whole column of the atmosphere over the BCES is generally warmed up by negative SIC-related anomalous heating. Q1 is further decomposed into three individual terms, namely, the sensible heat flux at the surface (Fig. 3b), the net radiation in an atmospheric column (Fig. 3c), and the latent heat flux–related condensation (Fig. 3d). Associated with negative SIC anomalies, the SH is enhanced, which is attributed to the increase in SST and decrease in SIC over the BCES (supplemental Figs. 1e and 2). In contrast to the SH, the RAD over BCES is negative, suggesting that less net radiation is absorbed by the column of the atmosphere (Fig. 3c). Weak positive COND anomalies can also be observed in part of the BCES region, indicating that the negative SIC anomalies have a limited effect on COND over BCES (Fig. 3d). In summary, Fig. 3 shows that negative BCES SIC anomalies impose a heating effect on the whole column of atmosphere over BCES. The magnitudes of the RAD and COND are obviously weaker than those of SH, while the enhanced SH has the largest contribution to this heating effect.

4. Impact of autumn BCES SIC variation on precipitation in NME

Previous sections show that the autumn BCES SIC anomalies can persist until the following early winter and that the SIC anomalies impose a heating effect on the overlying column of the atmosphere. In this section, we examine the anomalous precipitation over NME in the following winter related to autumn BCES SIC variation.

a. Anomalous precipitation over NME related to autumn BCES SIC variation

To examine the possible link between the autumn BCES SIC and the precipitation over NME in the following seasons, the anomalous precipitation and column water vapor flux over NME from autumn to the following early winter are obtained by regression on IBCES and are depicted in Fig. 4. In autumn, associated with negative BCES SIC anomalies, significant positive precipitation anomalies are observed over a large area of Europe, while significant negative precipitation anomalies are observed over northern Europe and the mid- and high-latitude central Eurasian continent (Fig. 4a). The BCES SIC–related precipitation anomalies are intensified and extend eastward to the west Siberian plain in the following late autumn (Fig. 4c). In the following early winter, the precipitation anomalies become weak to some extent but remain significant over Europe and the central Eurasian continent (Fig. 4e).

The evolution of the BCES SIC–related precipitation anomalies is closely associated with the low-level wind anomalies. In autumn, an anomalous cyclone and anticyclone dominate east North Atlantic Ocean–south Europe and western Russia, respectively (Fig. 4a). Anomalous westerly and southeasterly winds along the south and east flanks of the anomalous cyclone transport moisture from the North Atlantic Ocean and Mediterranean Sea to the inner land, accompanied by significant water vapor convergence (Fig. 4b), leading to more precipitation over Europe (Fig. 4a). To the east, a branch of anomalous northerly and northeasterly winds along the eastern flank of the central Eurasian anticyclone brings drier and colder air from higher latitudes, accompanied by divergence of the water vapor flux, leading to negative precipitation anomalies over vast regions of central Eurasia and the west Siberian plain. The BCES SIC–related low-level circulation anomalies persist in late autumn (Figs. 4c,d) and early winter (Figs. 4e,f), consistent with the anomalous precipitation pattern.

In addition to the cyclone over the east North Atlantic Ocean–south Europe and the anticyclone over western Russia, another anomalous anticyclone can be noticed over the northwest North Atlantic Ocean centered over Iceland, forming a wave train–like pattern, suggesting that the atmospheric circulation anomalies over NME might originate from the high latitudes. To explore the link between the autumn BCES SIC anomalies and the early winter precipitation over NME, the 200-hPa geopotential height anomalies and the corresponding wave activity flux associated with the IBCES from autumn to the following early winter are presented in Fig. 5. Corresponding to negative SIC anomalies in BCES, in autumn, significant positive geopotential height anomalies emerge over BCES in the upper troposphere (Fig. 5a). Simultaneously, negative, positive, and negative geopotential height anomalies are observed over the downstream regions of North America, the North Atlantic, and the western Eurasian continent, respectively, forming a wave train–like pattern extending from BCES to NME (Fig. 5a). The IBCES-associated wave activity fluxes also emerge over BCES and propagate southeastward to the NME

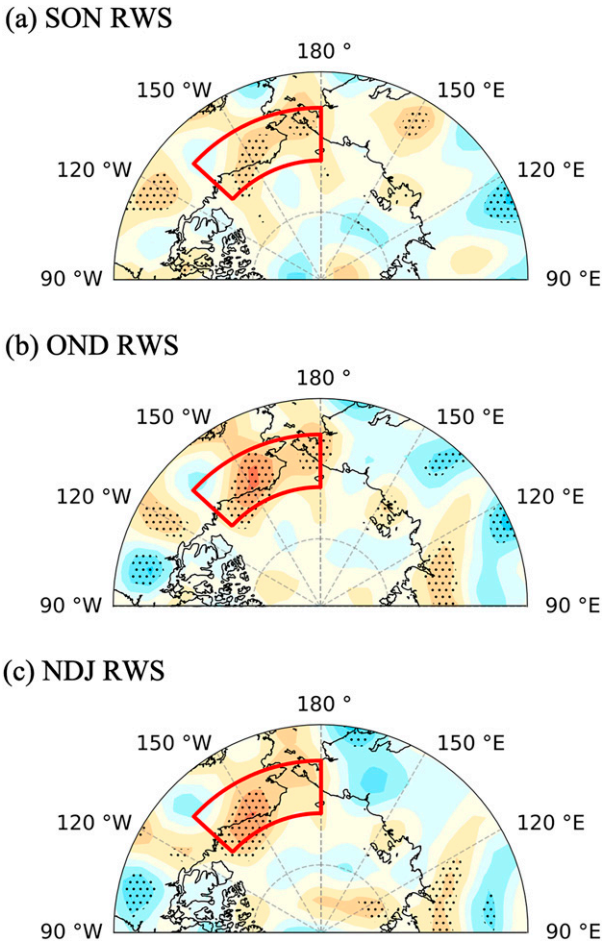

FIG. 8. Anomalies of (a) SON, (b) OND, and (c) NDJ Rossby wave sources (shading; scale factor of 10^{11}) obtained by linear regression onto the IBCES index. Stippled regions denote the 90% confidence level. Grid points in the red box (65.0°–72.5°N, 132.5°W–180.0°) are assigned with a perturbation in the Rossby wave ray tracing experiment.

(Fig. 5a). This wave train–like pattern persists and intensifies in the following late autumn and early winter (Figs. 5b,c). Along the path of the wave train, significant negative and positive geopotential height anomalies dominate east North Atlantic Ocean–south Europe and western Russia, which matches well with the anomalous cyclone and anticyclone systems over these regions, as shown in Fig. 4. This indicates that the BCES SIC–related circulation changes might contribute to the precipitation anomalies over NME in the following early winter.

To further understand the mechanisms of the development and maintenance of the BCES SIC–related atmospheric wave train pattern, the IBCES-related CP and CK are obtained by regression and are presented in Fig. 6. In autumn, associated with negative SIC anomalies in BCES, positive CP anomalies are noticed near BCES (Fig. 6a). Positive and negative CP anomalies are observed in North America and the North Atlantic Ocean downstream of BCES, with the path and pattern matching the propagation of the BCES SIC–related

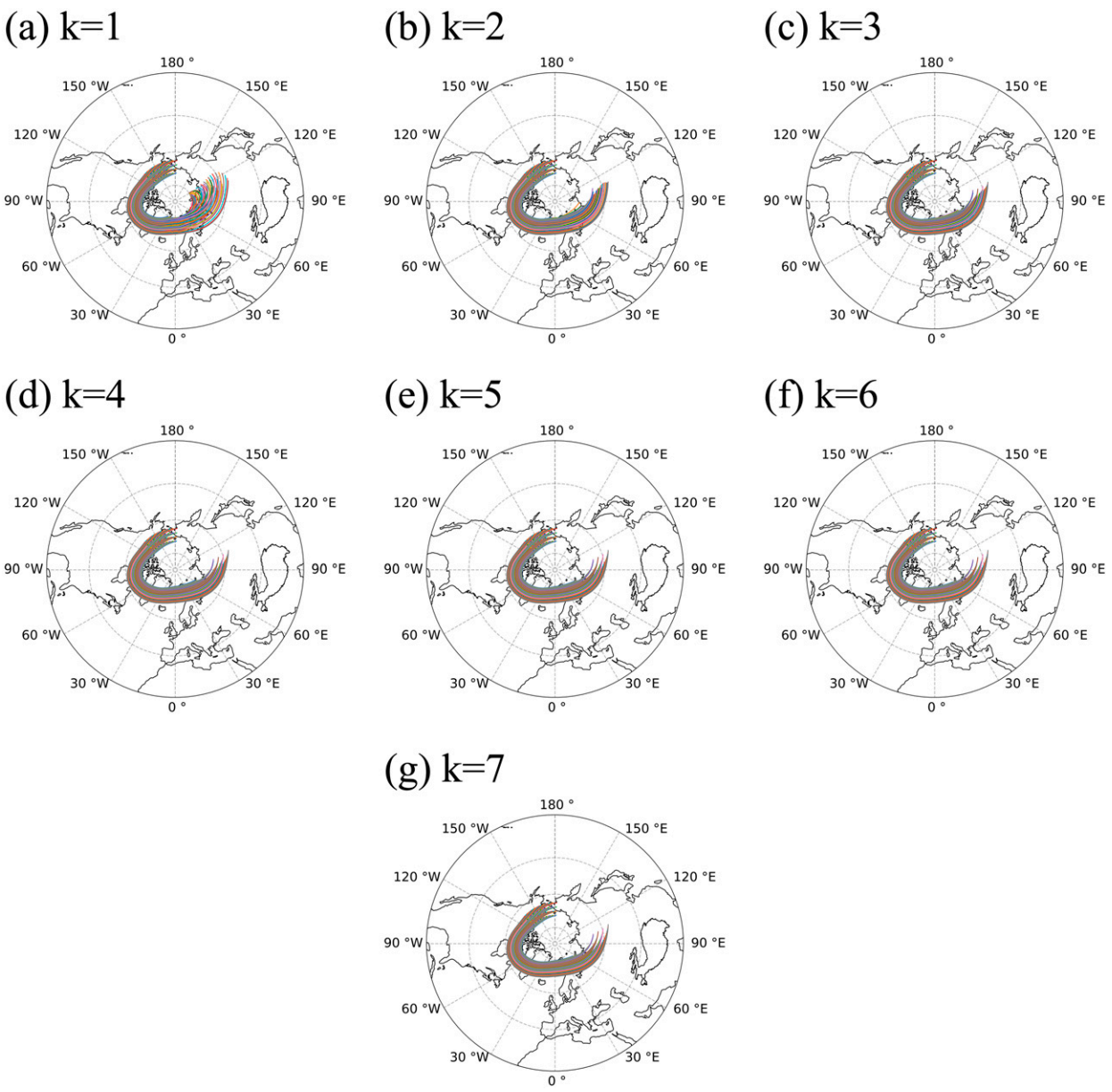

FIG. 9. The paths of eastward-propagating Rossby waves from the Arctic regions to the Eurasian continent, starting with an initial zonal wavenumber of (a) 1, (b) 2, (c) 3, (d) 4, (e) 5, (f) 6, and (g) 7 and following the waves for 20 days. Each line in the panels represents a ray path of one perturbation. For more details, please refer to the main text.

WAF (Fig. 6a). In contrast, the CK anomalies related to the BCES SIC variation are small (Fig. 6b), indicating that CP has a larger contribution to the development of the atmospheric wave pattern. Both CK and CP intensified in the following late autumn and early winter (Figs. 6c–f). The spatial distribution of CK and CP matches the wave centers shown in Fig. 5. This result indicates that both CK and CP might contribute to the autumn BCES SIC–related atmospheric wave pattern from autumn to early winter, while the effect of CP is much stronger than that of CK. This is consistent with supplemental Fig. 8 (section 2 of the supplemental material), which shows that the Eliassen–Palm (E–P) flux anomalies in the troposphere between 40° and 60°N have a larger vertical component than the horizontal component, suggesting that the heat flux is larger than the momentum flux.

In addition, there exists a time delay in the impacts of reduced autumn BCES SIC on winter NME precipitation. In addition to tropospheric wave–mean flow interactions, the stratospheric coupling process may also contribute to this phenomenon. The stratosphere–troposphere interaction is better captured by the time–height cross sections of the area-mean geopotential height anomaly over the Arctic region

(Fig. 7). The downward propagation of geopotential height anomalies begins in November and is maintained until March. Previous studies noted that the stratosphere–troposphere almost takes up 2 months of decorrelation time (Baldwin and Dunkerton 2001). Ding et al. (2021) also showed that there exists such a downward propagation of positive geopotential height anomalies from stratosphere to troposphere in winter due to the early autumn SIC anomalies over BCES. These results further support the analysis of this study. A more detailed discussion of the delay mechanism and analysis can be found in section 2 in the supplemental material.

b. *Rossby wave ray tracing experiment*

In this section, to verify the role of the BCES SIC forcing in the atmospheric wave pattern and the precipitation over the NME, a Rossby wave ray tracing experiment is performed to track the ray path of BCES SIC–related waves. Before the ray tracing experiment, we first examined the BCES SIC–related Rossby wave source anomalies (Fig. 8). Associated with negative BCES SIC anomalies, positive Rossby wave source anomalies appear near the Bering Strait and persist until early winter. According to this result, the perturbations in ray tracing experiments are placed near the Bering Strait (red box in Fig. 8).

The results of the Rossby wave ray tracing experiment are presented in Fig. 9. This shows that the perturbations near the Bering Strait can excite Rossby waves propagating eastward zonally and that the ray paths are consistent with the path of the atmospheric wave train, as shown in Fig. 5, confirming the relationship between the BCES SIC forcing and the atmospheric wave pattern. We also perform several other experiments by using the climatological means of 200-hPa horizontal velocities in late autumn and early winter as basic states. The results (section 3 in the supplemental material) are quite similar to those shown in Fig. 9, indicating that the basic states in the following late autumn and early winter change little. This result also confirms the robustness of our analysis. In summary, the ray tracing experiment shows that BCES SIC–related perturbations can produce an eastward-propagating Rossby wave, which can reach the NME regions and may affect the climate there.

c. *CAM experiments*

Associated with the autumn SIC forcing in BCES, a wave train pattern is observed in the model atmosphere dominating the BCES–North America–North Atlantic sector and the NME region (Fig. 10a). The wave pattern intensifies in the following late autumn and early winter (Figs. 10b,c). The negative and positive geopotential anomalies over east Atlantic Ocean–south Europe and over the central Eurasian continent are consistent with those in the observations (Fig. 5). The pattern correlation coefficient between Figs. 10c and 5c is 0.67, significant at the 90% confidence level. In addition, the propagation path of the Rossby wave in the model bears a high

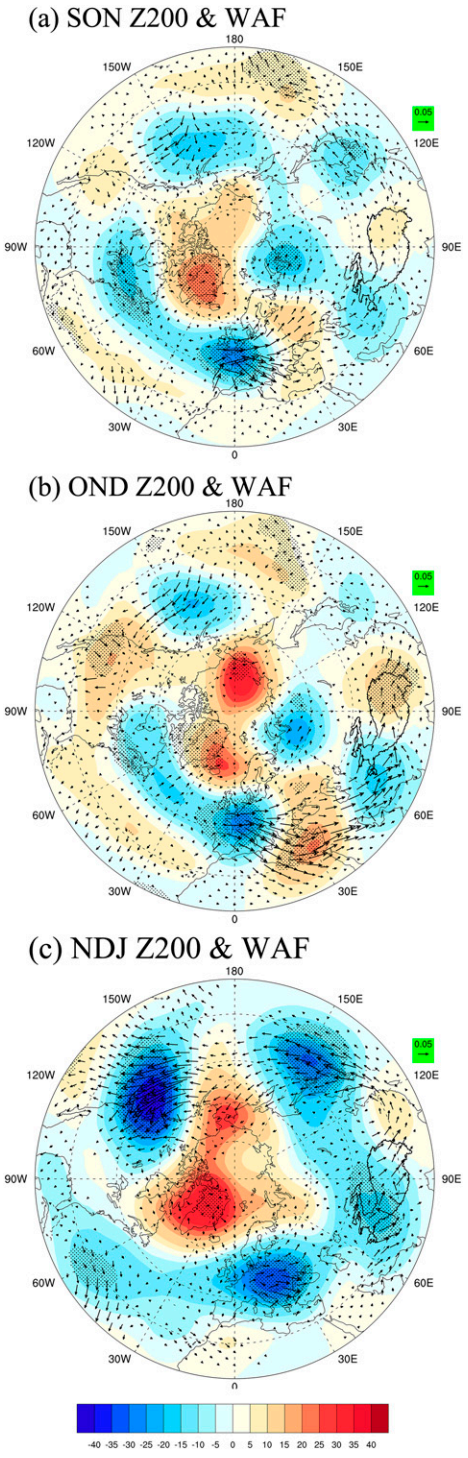

FIG. 10. Differences in the (a) SON, (b) OND, and (c) NDJ 200-hPa geopotential height (shading; unit: gpm) between the sensitivity experiment and the control experiment of CAM5 for the last 200 years of integration. The black vectors denote the corresponding wave activity flux (unit: $m^2\ s^{-2}$). Stippled regions represent anomalies significant at the 90% confidence level.

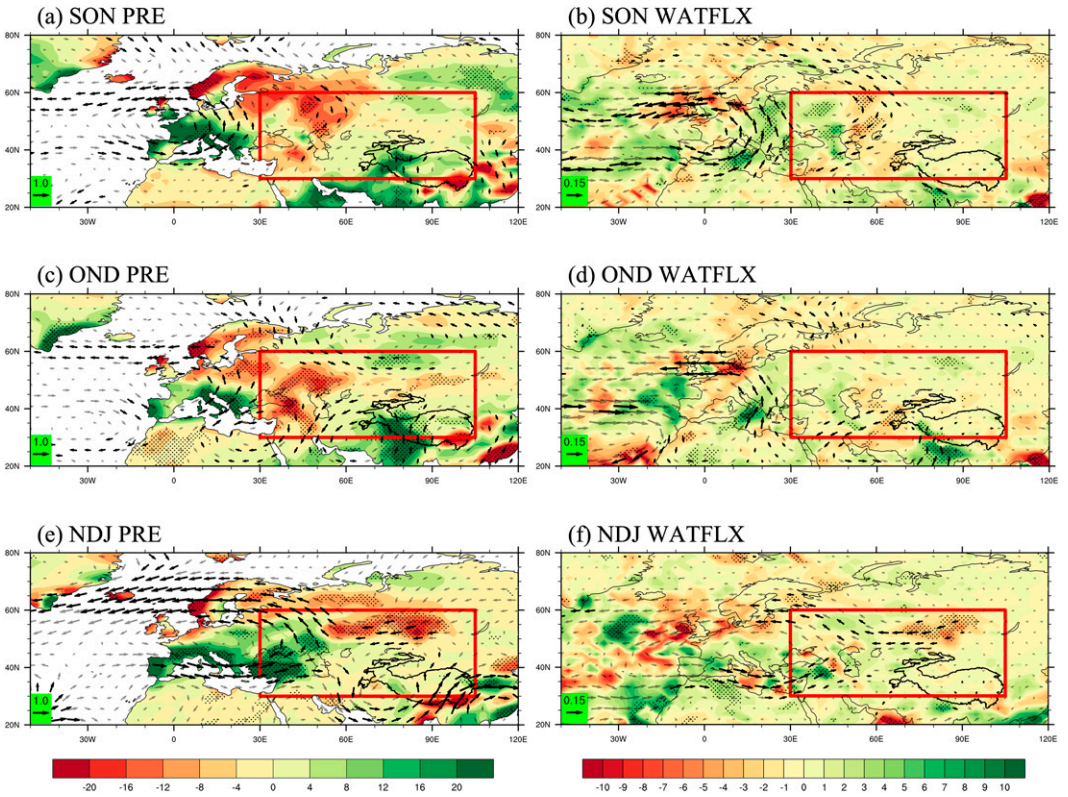

FIG. 11. Differences in the (a),(b) SON, (c),(d) OND, and (e),(f) NDJ (a),(c),(e) precipitation (shading; unit: mm) and 850-hPa wind (vectors; unit: m s^{-1}) and (b),(d),(f) column water vapor flux from 1000 to 10 hPa (vectors; unit: 10^2 kg·m^{-1}·s^{-1}) and corresponding divergence (shading; unit: 10^2 kg·m^{-1}·s^{-1}) between the sensitivity experiment and the control experiment of CAM5 for the last 200-yr integration. Stippled regions represent anomalies significant at the 90% confidence level. Black vectors represent vector anomalies significant at the 90% confidence level. The red rectangle box denotes the NME region (30°–60°N, 30°–105°E).

similarity to the ray tracing experiments and is also consistent with that in the observational analysis. The model responses of the precipitation, low-level wind, and column water vapor flux are shown in Fig. 11. In autumn, an anomalous cyclone (Figs. 11a,b) dominates the eastern Atlantic Ocean and western Europe, which brings moisture from the North Atlantic Ocean eastward to the continent. Water vapor flux convergence and positive precipitation anomalies are observed over southern Europe. Accompanying anomalous northeasterly winds over the central Eurasian continent, negative precipitation anomalies extend from northern Europe to central Asia and the west Siberian plain (Fig. 11a). The anomalous precipitation pattern and anomalous cyclone persist until early winter (Figs. 11c–f), which is also consistent with the observational analyses (Fig. 4). Some differences between the numerical experimental results and the observations can also be noticed. For example, in NDJ, the simulated anomalous cyclone over Europe shifts slightly toward the west compared to the observations. This discrepancy may be due to the effect of model bias or other factors or processes.

In summary, the results of Rossby wave ray tracing and CAM sensitivity experiments share many similarities to those in the observations. This confirms that negative autumn SIC anomalies in BCES can excite a large-scale wave train–like atmospheric pattern that crosses North America and the North Atlantic and reaches the NME region and can affect the variation in early winter precipitation over NME.

5. Summary

In this study, we investigate the mechanisms of the impact imposed by anomalous autumn sea ice in BCES on early winter precipitation over NME with a focus on the interannual variations. The leading EOF mode of SIC variation in the Arctic Ocean shows large loading in BCES, which is also the region with large SIC interannual variations. Local budget analysis shows that negative SIC anomalies in BCES play a heating role in the overlying atmosphere and cause a warming of the above air. Further analysis shows that associated with anomalous negative SIC, a branch of Rossby waves is induced. The wave propagates downstream, crossing North America and the North Atlantic and reaching NME, and this wave pattern can persist until early winter. A low-level anomalous cyclone and anticyclone are observed over Europe and the central Eurasian continent associated with this wave pattern, causing significant precipitation anomalies in early winter over vast regions in NME. The Rossby wave ray tracing and CAM numerical

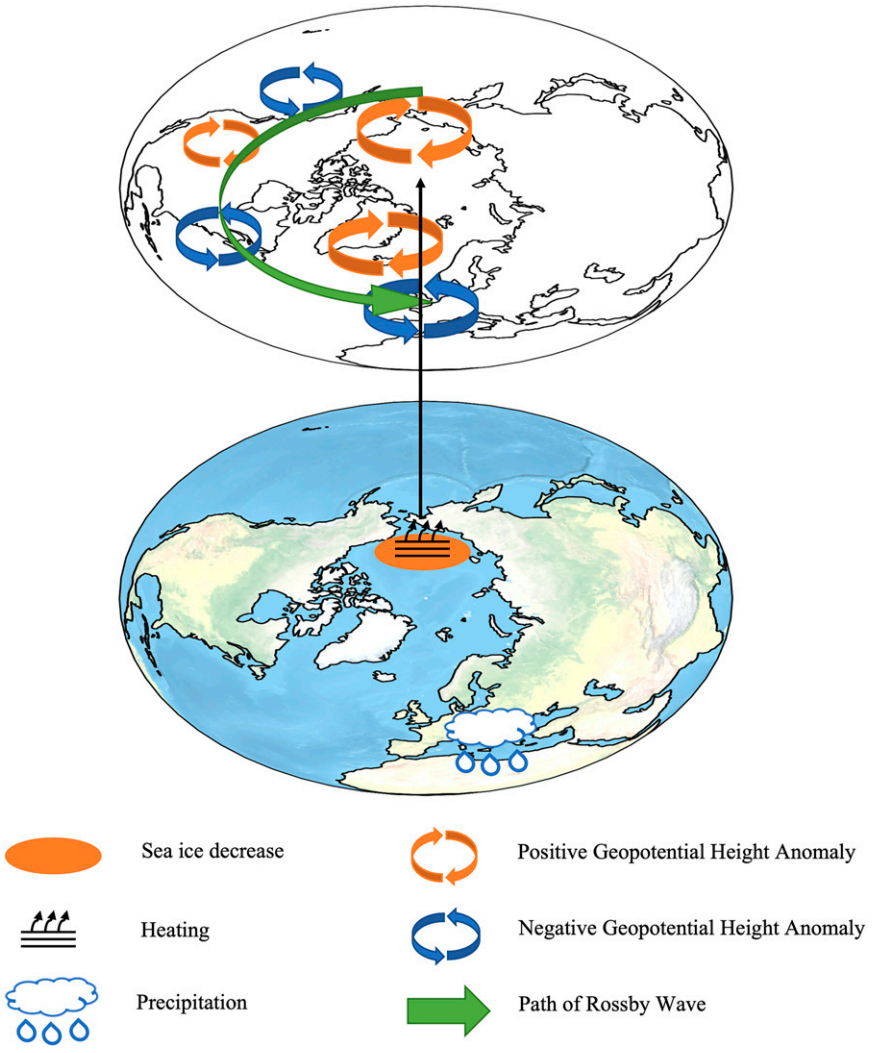

FIG. 12. Schematic representation of the climate effect of sea ice decrease on early winter precipitation over the nonmonsoonal Eurasian continent.

experiment support this mechanism. Figure 12 summarizes the processes of the BCES SIC–NME precipitation relationship.

Compared with previous studies focusing on the SIC impact on temperatures and extreme cold events, this work revealed that autumn SIC over BCES can affect early winter precipitation over NME. The results, together with our previous work (Qian et al. 2021), demonstrate that improving the Arctic sea ice–atmosphere interaction process in climate models is important and may be efficient in helping improve the seasonal forecast skill of operational numerical models over the NME regions. In addition, previous studies revealed that Arctic sea ice is decreasing, including in the BCES region, especially in autumn. How the BCES SIC–NME precipitation relationship will change under the background of global warming needs further investigation and will be addressed in our next study.

Acknowledgments. This research is funded by the National Natural Science Foundation of China (Grants 42205020 and 42075050) and the Zhejiang Provincial Natural Science Foundation of China under Grant LQ23D050003. Thanks to Dr. Shuoyi Ding at Fudan University for providing us instructions for the calculation of some diagnostics.

Data availability statement. The CRU land rainfall data can be obtained from https://www.uea.ac.uk/groups-and-centres/climatic-research-unit. The Hadley SST and SIC data can be accessed from https://www.metoffice.gov.uk/hadobs/index.html. The NCEP–DOE AMIP-II reanalysis datasets can be downloaded from https://psl.noaa.gov/data/gridded/.

REFERENCES

Alexander, M. A., U. S. Bhatt, J. E. Walsh, M. S. Timlin, J. S. Miller, and J. D. Scott, 2004: The atmospheric response to realistic Arctic sea ice anomalies in an AGCM during winter. *J. Climate*, **17**, 890–905, https://doi.org/10.1175/1520-0442(2004)017<0890:TARTRA>2.0.CO;2.

An, Z., and Coauthors, 2015: Global monsoon dynamics and climate change. *Annu. Rev. Earth Planet. Sci.*, **43**, 29–77, https://doi.org/10.1146/annurev-earth-060313-054623.

Baldwin, M. P., and T. J. Dunkerton, 2001: Stratospheric harbingers of anomalous weather regimes. *Science*, **294**, 581–584, https://doi.org/10.1126/science.1063315.

Blackport, R., and J. A. Screen, 2019: Influence of Arctic sea ice loss in autumn compared to that in winter on the atmospheric circulation. *Geophys. Res. Lett.*, **46**, 2213–2221, https://doi.org/10.1029/2018GL081469.

Bretherton, C. S., and S. Park, 2009: A new moist turbulence parameterization in the community atmosphere model. *J. Climate*, **22**, 3422–3448, https://doi.org/10.1175/2008JCLI2556.1.

——, M. Widmann, V. P. Dymnikov, J. M. Wallace, and I. Bladé, 1999: The effective number of spatial degrees of freedom of a time-varying field. *J. Climate*, **12**, 1990–2009, https://doi.org/10.1175/1520-0442(1999)012<1990:TENOSD>2.0.CO;2.

Budikova, D., 2009: Role of Arctic sea ice in global atmospheric circulation: A review. *Global Planet. Change*, **68**, 149–163, https://doi.org/10.1016/j.gloplacha.2009.04.001.

Chen, F., J. Wang, L. Jin, Q. Zhang, J. Li, and J. Chen, 2009: Rapid warming in mid-latitude central Asia for the past 100 years. *Front. Earth Sci. China*, **3**, 42–50, https://doi.org/10.1007/s11707-009-0013-9.

Chen, S., and R. Wu, 2018: Impacts of early autumn Arctic sea ice concentration on subsequent spring Eurasian surface air temperature variations. *Climate Dyn.*, **51** 2523–2542, https://doi.org/10.1007/s00382-017-4026-x.

——, ——, and Y. Liu, 2016: Dominant modes of interannual variability in Eurasian surface air temperature during boreal spring. *J. Climate*, **29**, 1109–1125, https://doi.org/10.1175/JCLI-D-15-0524.1.

Chen, Z., R. Wu, and W. Chen, 2014: Impacts of autumn Arctic sea ice concentration changes on the East Asian winter monsoon variability. *J. Climate*, **27**, 5433–5450, https://doi.org/10.1175/JCLI-D-13-00731.1.

Christensen, J. H., and Coauthors, 2013: Climate phenomena and their relevance for future regional climate change. *Climate Change 2013: The Physical Science Basis*, T. F. Stocker et al., Eds., Cambridge University Press, 1217–1308.

Curry, J. A., J. L. Schramm, and E. E. Ebert, 1995: Sea ice–albedo climate feedback mechanism. *J. Climate*, **8**, 240–247, https://doi.org/10.1175/1520-0442(1995)008<0240:SIACFM>2.0.CO;2.

Deser, C., J. E. Walsh, and M. S. Timlin, 2000: Arctic sea ice variability in the context of recent atmospheric circulation trends. *J. Climate*, **13**, 617–633, https://doi.org/10.1175/1520-0442(2000)013<0617:ASIVIT>2.0.CO;2.

Dethloff, K., and Coauthors, 2006: A dynamical link between the Arctic and the global climate system. *Geophys. Res. Lett.*, **33**, L03703, https://doi.org/10.1029/2005GL025245.

Ding, S., B. Wu, and W. Chen, 2021: Dominant characteristics of early autumn Arctic sea ice variability and its impact on winter Eurasian climate. *J. Climate*, **34**, 1825–1846, https://doi.org/10.1175/JCLI-D-19-0834.1.

Fallah, B., S. Sodoudi, and U. Cubasch, 2016: Westerly jet stream and past millennium climate change in arid central Asia simulated by COSMO-CLM model. *Theor. Appl. Climatol.*, **124**, 1079–1088, https://doi.org/10.1007/s00704-015-1479-x.

Francis, J. A., and S. J. Vavrus, 2012: Evidence linking Arctic amplification to extreme weather in mid-latitudes. *Geophys. Res. Lett.*, **39**, L06801, https://doi.org/10.1029/2012GL051000.

——, and ——, 2015: Evidence for a wavier jet stream in response to rapid Arctic warming. *Environ. Res. Lett.*, **10**, 014005, https://doi.org/10.1088/1748-9326/10/1/014005.

——, W. Chan, D. J. Leathers, J. R. Miller, and D. E. Veron, 2009: Winter Northern Hemisphere weather patterns remember summer Arctic sea-ice extent. *Geophys. Res. Lett.*, **36**, L07503, https://doi.org/10.1029/2009GL037274.

Gao, Y., and Coauthors, 2015: Arctic sea ice and Eurasian climate: A review. *Adv. Atmos. Sci.*, **32**, 92–114, https://doi.org/10.1007/s00376-014-0009-6.

Giorgi, F., 2006: Climate change hot-spots. *Geophys. Res. Lett.*, **33**, L08707, https://doi.org/10.1029/2006GL025734.

Harris, I., P. D. Jones, T. J. Osborn, and D. H. Lister, 2014: Updated high-resolution grids of monthly climatic observations—The CRU TS3.10 dataset. *Int. J. Climatol.*, **34**, 623–642, https://doi.org/10.1002/joc.3711.

He, X., R. Zhang, S. Ding, and Z. Zuo, 2022: Interdecadal linkage between the winter Northern Hemisphere climate and Arctic sea ice of diverse location and seasonality. *Front. Earth Sci.*, **9**, 758619, https://doi.org/10.3389/feart.2021.758619.

Hopsch, S., J. Cohen, and K. Dethloff, 2012: Analysis of a link between fall Arctic sea ice concentration and atmospheric patterns in the following winter. *Tellus*, **64A**, 18624, https://doi.org/10.3402/tellusa.v64i0.18624.

Hu, Z., Q. Li, X. Chen, Z. Teng, C. Chen, G. Yin, and Y. Zhang, 2016: Climate changes in temperature and precipitation extremes in an alpine grassland of central Asia. *Theor. Appl. Climatol.*, **126**, 519–531, https://doi.org/10.1007/s00704-015-1568-x.

Huang, A., Y. Zhou, Y. Zhang, D. Huang, Y. Zhao, and H. Wu, 2014: Changes of the annual precipitation over central Asia in the twenty-first century projected by multimodels of CMIP5. *J. Climate*, **27**, 6627–6646, https://doi.org/10.1175/JCLI-D-14-00070.1.

Huang, J., X. Guan, and F. Ji, 2012: Enhanced cold-season warming in semi-arid regions. *Atmos. Chem. Phys.*, **12**, 5391–5398, https://doi.org/10.5194/acp-12-5391-2012.

——, H. Yu, X. Guan, G. Wang, and R. Guo, 2016: Accelerated dryland expansion under climate change. *Nat. Climate Change*, **6**, 166–171, https://doi.org/10.1038/nclimate2837.

Iacono, M. J., J. S. Delamere, E. J. Mlawer, M. W. Shephard, S. A. Clough, and W. D. Collins, 2008: Radiative forcing by long-lived greenhouse gases: Calculations with the AER radiative transfer models. *J. Geophys. Res.*, **113**, D13103, https://doi.org/10.1029/2008JD009944.

IPCC, 2019: *The Ocean and Cryosphere in a Changing Climate*. Cambridge University Press, 765 pp.

Jaiser, R., K. Dethloff, D. Handorf, A. Rinke, and J. Cohen, 2012: Impact of sea ice cover changes on the Northern Hemisphere atmospheric winter circulation. *Tellus*, **64A**, 11595, https://doi.org/10.3402/tellusa.v64i0.11595.

Jia, X., D. R. Cao, J. W. Ge, and M. Wang, 2018: Interdecadal change of the impact of Eurasian snow on spring precipitation over southern China. *J. Geophys. Res. Atmos.*, **123**, 10 092–10 108, https://doi.org/10.1029/2018JD028612.

Jiang, J., T. Zhou, X. Chen, and L. Zhang, 2020: Future changes in precipitation over central Asia based on CMIP6 projections. *Environ. Res. Lett.*, **15**, 054009, https://doi.org/10.1088/1748-9326/ab7d03.

Kanamitsu, M., W. Ebisuzaki, J. Woollen, S.-K. Yang, J. J. Hnilo, M. Fiorino, and G. L. Potter, 2002: NCEP-DOE AMIP-II reanalysis (R-2). *Bull. Amer. Meteor. Soc.*, **83**, 1631–1644, https://doi.org/10.1175/BAMS-83-11-1631.

Karoly, D. J., 1983: Rossby wave propagation in a barotropic atmosphere. *Dyn. Atmos. Oceans*, **7**, 111–125, https://doi.org/10.1016/0377-0265(83)90013-1.

Kosaka, Y., and H. Nakamura, 2006: Structure and dynamics of the summertime Pacific–Japan teleconnection pattern. *Quart. J. Roy. Meteor. Soc.*, **132**, 2009–2030, https://doi.org/10.1256/qj.05.204.

Li, F., and H. Wang, 2012: Autumn sea ice cover, winter Northern Hemisphere annular mode, and winter precipitation in Eurasia. *J. Climate*, **26**, 3968–3981, https://doi.org/10.1175/JCLI-D-12-00380.1.

Li, J. P., and Q. C. Zeng, 2005: A new monsoon index, its interannual variability and relation with monsoon precipitation (in Chinese). *Climatic Environ. Res.*, **10**, 351–365, https://doi.org/10.3878/j.issn.1006-9585.2005.03.09.

Li, X., D. M. Holland, E. P. Gerber, and C. Yoo, 2015: Rossby waves mediate impacts of tropical oceans on west Antarctic atmospheric circulation in austral winter. *J. Climate*, **28**, 8151–8164, https://doi.org/10.1175/JCLI-D-15-0113.1.

Liu, J., J. A. Curry, H. Wang, M. Song, and R. M. Horton, 2012: Impact of declining Arctic sea ice on winter snowfall. *Proc. Natl. Acad. Sci. USA*, **109**, 4074–4079, https://doi.org/10.1073/pnas.1114910109.

Morrison, H., and A. Gettelman, 2008: A new two-moment bulk stratiform cloud microphysics scheme in the Community Atmosphere Model, version 3 (CAM3). Part I: Description and numerical tests. *J. Climate*, **21**, 3642–3659, https://doi.org/10.1175/2008JCLI2105.1.

Nakamura, T., K. Yamazaki, K. Iwamoto, M. Honda, Y. Miyoshi, Y. Ogawa, and J. Ukita, 2015: A negative phase shift of the winter AO/NAO due to the recent Arctic sea-ice reduction in late autumn. *J. Geophys. Res. Atmos.*, **120**, 3209–3227, https://doi.org/10.1002/2014JD022848.

Neale, R. B., and Coauthors, 2010: Description of the NCAR Community Atmosphere Model (CAM 5.0). NCAR Tech. Note NCAR/TN-486+STR, 268 pp., www.cesm.ucar.edu/models/cesm1.1/cam/docs/description/cam5_desc.pdf.

North, G. R., T. L. Bell, R. F. Cahalan, and F. J. Moeng, 1982: Sampling errors in the estimation of empirical orthogonal functions. *Mon. Wea. Rev.*, **110**, 699–706, https://doi.org/10.1175/1520-0493(1982)110<0699:SEITEO>2.0.CO;2.

Ogawa, F., and Coauthors, 2018: Evaluating impacts of recent Arctic sea ice loss on the Northern Hemisphere winter climate change. *Geophys. Res. Lett.*, **45**, 3255–3263, https://doi.org/10.1002/2017GL076502.

Park, S., and C. S. Bretherton, 2009: The University of Washington shallow convection and moist turbulence schemes and their impact on climate simulations with the Community Atmosphere Model. *J. Climate*, **22**, 3449–3469, https://doi.org/10.1175/2008JCLI2557.1.

——, ——, and P. J. Rasch, 2014: Integrating cloud processes in the Community Atmosphere Model, version 5. *J. Climate*, **27**, 6821–6856, https://doi.org/10.1175/JCLI-D-14-00087.1.

Peings, Y., and G. Magnusdottir, 2014: Response of the wintertime Northern Hemisphere atmospheric circulation to current and projected Arctic sea ice decline: A numerical study with CAM5. *J. Climate*, **27**, 244–264, https://doi.org/10.1175/JCLI-D-13-00272.1.

——, Z. M. Labe, and G. Magnusdottir, 2021: Are 100 ensemble members enough to capture the remote atmospheric response to +2°C Arctic sea ice loss? *J. Climate*, **34**, 3751–3769, https://doi.org/10.1175/JCLI-D-20-0613.1.

Peng, D., T. Zhou, L. Zhang, W. Zhang, and X. Chen, 2020: Observationally constrained projection of the reduced intensification of extreme climate events in central Asia from 0.5°C less global warming. *Climate Dyn.*, **54**, 543–560, https://doi.org/10.1007/s00382-019-05014-6.

Qian, Q., X. Jia, H. Lin, and R. Zhang, 2021: Seasonal forecast of nonmonsoonal winter precipitation over the Eurasian continent using machine-learning models. *J. Climate*, **34**, 7113–7129, https://doi.org/10.1175/JCLI-D-21-0113.1.

Rayner, N. A., D. E. Parker, E. B. Horton, C. K. Folland, L. V. Alexander, D. P. Rowell, E. C. Kent, and A. Kaplan, 2003: Global analyses of sea surface temperature, sea ice, and night marine air temperature since the late nineteenth century. *J. Geophys. Res.*, **108**, 4407, https://doi.org/10.1029/2002JD002670.

Sardeshmukh, P. D., and B. J. Hoskins, 1988: The generation of global rotational flow by steady, idealized tropical divergence. *J. Atmos. Sci.*, **45**, 1228–1251, https://doi.org/10.1175/1520-0469(1988)045<1228:TGOGRF>2.0.CO;2.

Serreze, M. C., M. M. Holland, and J. Stroeve, 2007: Perspectives on the Arctic's shrinking sea-ice cover. *Science*, **315**, 1533–1536, https://doi.org/10.1126/science.1139426.

Shaman, J., and E. Tziperman, 2005: The effect of ENSO on Tibetan Plateau snow depth: A stationary wave teleconnection mechanism and implications for the South Asian monsoons. *J. Climate*, **18**, 2067–2079, https://doi.org/10.1175/JCLI3391.1.

Siew, P. Y. F., C. Li, S. P. Sobolowski, and M. P. King, 2020: Intermittency of Arctic–mid-latitude teleconnections: Stratospheric pathway between autumn sea ice and the winter North Atlantic Oscillation. *Wea. Climate Dyn.*, **1**, 261–275, https://doi.org/10.5194/wcd-1-261-2020.

Smith, D. M., and Coauthors, 2019: The Polar Amplification Model Intercomparison Project (PAMIP) contribution to CMIP6: Investigating the causes and consequences of polar amplification. *Geosci. Model Dev.*, **12**, 1139–1164, https://doi.org/10.5194/gmd-12-1139-2019.

Sorg, A., T. Bolch, M. Stoffel, O. Solomina, and M. Beniston, 2012: Climate change impacts on glaciers and runoff in Tien Shan (central Asia). *Nat. Climate Change*, **2**, 725–731, https://doi.org/10.1038/nclimate1592.

Stroeve, J., and D. Notz, 2018: Changing state of Arctic sea ice across all seasons. *Environ. Res. Lett.*, **13**, 103001, https://doi.org/10.1088/1748-9326/aade56.

Sun, L., C. Deser, and R. A. Tomas, 2015: Mechanisms of stratospheric and tropospheric circulation response to projected Arctic sea ice loss. *J. Climate*, **28**, 7824–7845, https://doi.org/10.1175/JCLI-D-15-0169.1.

Takaya, K., and H. Nakamura, 2001: A formulation of a phase-independent wave-activity flux for stationary and migratory quasigeostrophic eddies on a zonally varying basic flow. *J. Atmos. Sci.*, **58**, 608–627, https://doi.org/10.1175/1520-0469(2001)058<0608:AFOAPI>2.0.CO;2.

Tang, Q., X. Zhang, X. Yang, and J. A. Francis, 2013: Cold winter extremes in northern continents linked to Arctic sea ice loss. *Environ. Res. Lett.*, **8**, 014036, https://doi.org/10.1088/1748-9326/8/1/014036.

Vihma, T., and Coauthors, 2020: Effects of the tropospheric large-scale circulation on European winter temperatures during the period of amplified Arctic warming. *Int. J. Climatol.*, **40**, 509–529, https://doi.org/10.1002/joc.6225.

Wang, C., K. Yang, Y. Li, D. Wu, and Y. Bo, 2017: Impacts of spatiotemporal anomalies of Tibetan Plateau snow cover on summer precipitation in eastern China. *J. Climate*, **30**, 885–903, https://doi.org/10.1175/JCLI-D-16-0041.1.

Wang, M., X. J. Jia, J. W. Ge, and Q. F. Qian, 2019: Changes in the relationship between the interannual variation of Eurasian snow

cover and spring SAT over eastern Eurasia. *J. Geophys. Res. Atmos.*, **124**, 468–487, https://doi.org/10.1029/2018JD029077.

Wu, B., J. Su, and R. Zhang, 2011: Effects of autumn-winter Arctic sea ice on winter Siberian high. *Chin. Sci. Bull.*, **56**, 3220–3228, https://doi.org/10.1007/s11434-011-4696-4.

——, D. Handorf, K. Dethloff, A. Rinke, and A. Hu, 2013: Winter weather patterns over northern Eurasia and Arctic sea ice loss. *Mon. Wea. Rev.*, **141**, 3786–3800, https://doi.org/10.1175/MWR-D-13-00046.1.

——, K. Yang, and J. A. Francis, 2017: A cold event in Asia during January–February 2012 and its possible association with Arctic sea ice loss. *J. Climate*, **30**, 7971–7990, https://doi.org/10.1175/JCLI-D-16-0115.1.

Wu, Z., P. Zhang, H. Chen, and Y. Li, 2016: Can the Tibetan Plateau snow cover influence the interannual variations of Eurasian heat wave frequency? *Climate Dyn.*, **46**, 3405–3417, https://doi.org/10.1007/s00382-015-2775-y.

Yao, J., and Y. Chen, 2015: Trend analysis of temperature and precipitation in the Syr Darya basin in central Asia. *Theor. Appl. Climatol.*, **120**, 521–531, https://doi.org/10.1007/s00704-014-1187-y.

Yiu, Y. Y. S., and A. C. Maycock, 2019: On the seasonality of the El Niño teleconnection to the Amundsen Sea region. *J. Climate*, **32**, 4829–4845, https://doi.org/10.1175/JCLI-D-18-0813.1.

——, and ——, 2020: The linearity of the El Niño teleconnection to the Amundsen Sea region. *Quart. J. Roy. Meteor. Soc.*, **146**, 1169–1183, https://doi.org/10.1002/qj.3731.

Zhang, G. J., and N. A. McFarlane, 1995: Sensitivity of climate simulations to the parameterization of cumulus convection in the Canadian Climate Centre General Circulation Model. *Atmos.–Ocean*, **33**, 407–446, https://doi.org/10.1080/07055900.1995.9649539.

Zhang, R., and J. A. Screen, 2021: Diverse Eurasian winter temperature responses to Barents–Kara Sea ice anomalies of different magnitudes and seasonality. *Geophys. Res. Lett.*, **48**, e2021GL092726, https://doi.org/10.1029/2021GL092726.

Zhang, Y., X. Kuang, W. Guo, and T. Zhou, 2006: Seasonal evolution of the upper-tropospheric westerly jet core over East Asia. *Geophys. Res. Lett.*, **33**, L11708, https://doi.org/10.1029/2006GL026377.

Zhao, P., and L. Chen, 2001: Climatic features of atmospheric heat source/sink over the Qinghai–Xizang Plateau in 35 years and its relation to rainfall in China. *Sci. China*, **44D**, 858–864, https://doi.org/10.1007/BF02907098.

Zhao, Y., A. Huang, Y. Zhou, D. Huang, Q. Yang, Y. Ma, M. Li, and G. Wei, 2014: Impact of the middle and upper tropospheric cooling over central Asia on the summer rainfall in the Tarim basin, China. *J. Climate*, **27**, 4721–4732, https://doi.org/10.1175/JCLI-D-13-00456.1.